Scanning angle interference microscopy reveals cell dynamics at the nanoscale

Matthew J Paszek[1,2], Christopher C DuFort[1,2], Matthew G Rubashkin[1,2], Michael W Davidson[3,4], Kurt S Thorn[5], Jan T Liphardt[2,6,7] & Valerie M Weaver[1,2,8–11]

Emerging questions in cell biology necessitate nanoscale imaging in live cells. Here we present scanning angle interference microscopy, which is capable of localizing fluorescent objects with nanoscale precision along the optical axis in motile cellular structures. We use this approach to resolve nanotopographical features of the cell membrane and cytoskeleton as well as the temporal evolution, three-dimensional architecture and nanoscale dynamics of focal adhesion complexes.

Real-time imaging with nanoscale precision remains challenging, especially along the optical axis. Current techniques (reviewed in ref. 1) have revealed the architecture of molecular complexes, such as focal adhesions in fixed cells, with unprecedented detail, yet the dynamic behavior of these structures remains largely unknown[2]. A need still exists for imaging methodologies capable of recording nanoscale structural details and movements in living cells, such as those occurring during processes such as motility[3–5].

The leading approach for measuring the topography of lipid membranes with nanoscale z-resolution is fluorescence interference contrast microscopy (FLIC)[6]. In FLIC, axially varying structured illumination is used to determine the vertical position of nanometer-sized objects. To eliminate periodic replication artifacts and obtain unambiguous positions, the pattern of structured illumination is manipulated by varying the angle of incidence of excitation light to provide additional spatial information[7]. Although FLIC has the potential to visualize the rapid movements and spatial organization of proteins, interference contrast

methodologies have not been widely adopted in biology, most likely because of the technical challenges of implementation and the assumptions that must be made regarding fluorophore molecular orientation.

Here we modify FLIC to develop a new interference contrast method with nanometer precision, which we term scanning angle interference microscopy. This approach can be implemented on commercial total internal reflection (TIRF) microscopes with no hardware modifications (**Supplementary Note**). We determine unambiguous positions of fluorescent structures over a wide axial range (approaching a micron or more) by actively scanning the incidence angle of the excitation. Furthermore, by manipulating the polarization state of light, we eliminated the requirement for knowledge of the orientation of fluorescence dipoles in the labeled structure. This approach enables imaging with nanoscale axial precision and temporal sampling rates on the order of one second.

Samples for scanning angle interference microscopy are prepared on reflective silicon wafers with a thin layer of silicon oxide (**Fig. 1a**). Axially varying patterns of excitation light intensity are generated through the interference of incident and reflected light, and the structure of the pattern is manipulated by controlling the incidence angle. To quantify performance, we adsorbed nanosized fluorescent beads on silicon substrates with oxide spacer layers of varying thickness and scanned them with excitation light of varying incidence angle. The recorded fluorescence intensity profiles were then fit to an optical model to obtain the axial position of the bead center from the silicon surface with nanoscale precision. The use of excitation light linearly polarized perpendicular to the plane of incidence (s-polarized) improved interference intensity contrast by as much as five-fold over nonpolarized or circularly polarized light (**Supplementary Fig. 1**), eliminated the dependence of the optical model on fluorophore dipole orientation (Online Methods) and improved the accuracy of object localization (**Supplementary Fig. 1**).

Measured bead heights above the silicon were, on average, within a few nanometers of expected heights based on thin film measurements of the silicon oxide (**Fig. 1b–d** and **Supplementary Fig. 2**), with the s.d. ranging from 3.6–5.1 nm (**Fig. 1d**). Beads varying in axial position by as little as 13 nm had distinct interference contrast profiles, allowing us to resolve their height differences (**Fig. 1b,c**). Similarly, analysis of mCherry and mEmerald conjugates of the focal adhesion protein paxillin in cells positioned

[1]Deparment of Surgery and Center for Bioengineering and Tissue Regeneration, University of California–San Francisco, San Francisco, California, USA. [2]Bay Area Physical Sciences–Oncology Center, University of California–Berkeley, Berkeley California, USA. [3]National High Magnetic Field Laboratory, The Florida State University, Tallahassee, Florida, USA. [4]Department of Biological Sciences, The Florida State University, Tallahassee, Florida, USA. [5]Department of Biochemistry and Biophysics, University of California–San Francisco, San Francisco, California, USA. [6]Department of Physics, University of California–Berkeley, Berkeley, California, USA. [7]QB3–California Institute for Quantitative Biosciences, University of California–Berkeley, Berkeley, California, USA. [8]Department of Anatomy, University of California–San Francisco, San Francisco, California, USA. [9]Department of Bioengineering and Therapeutic Sciences, University of California–San Francisco, San Francisco, California, USA. [10]Eli and Edythe Broad Center for Regeneration Medicine and Stem Cell Research, University of California–San Francisco, San Francisco, California, USA. [11]Helen Diller Family Comprehensive Cancer Center, University of California–San Francisco, San Francisco, California, USA. Correspondence should be addressed to V.M.W. (valerie.weaver@ucsfmedctr.org).
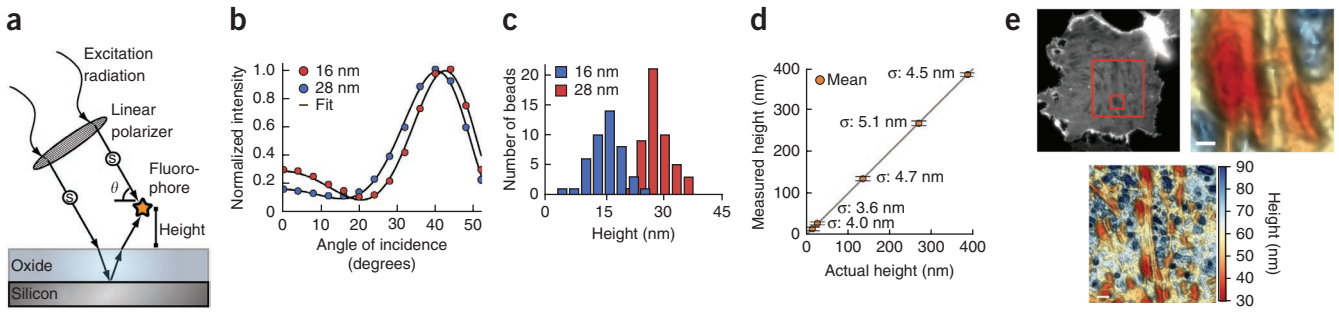
Figure 1 | Scanning angle interference microscopy. (**a**) Axially varying excitation intensity arises from interference between direct and reflected light off a silicon substrate. The structure of the illumination pattern is controlled by varying the polarization and angle of incidence of the excitation light and is manipulated to probe the height of a fluorophore above a reflective substrate. A thin layer of oxide is used to space the sample above the silicon surface. (**b**,**c**) Average emission intensity and fit to the optical model for beads at the indicated axial positions (**b**) and the corresponding histograms of axial position measured for individual beads (**c**). (**d**) Measured axial position of fluorescent beads adsorbed on silicon oxide layers of varying thickness plotted against their expected position. Error bars, s.d. (σ; $n = 45$–50). Height is reported as the axial distance of the bead center above the reference point $z = 500$ nm. (**e**) Epifluorescence image (top left) and three-dimensional scanning angle interference reconstruction (top right shows zoomed image; bottom shows topography of region of interest (ROI)) of an epithelial cell ventral membrane labeled with green fluorescent DiO (3,3′-dioctadecyloxacarbocyanine perchlorate). Boxes in the epifluorescence image indicate regions shown in ROI (larger box) and zoomed image (smaller box). Height is reported as the absolute distance of the membrane above the silicon oxide surface. Scale bars: bottom, 2 µm; top right, 750 nm.

at four heights above the silicon substrate revealed a s.d. of 1.8 nm from the mean height across eight independent measurements (**Supplementary Fig. 3**). We found that a signal-to-noise ratio of ~2 or more yielded the most accurate results in cellular samples (**Supplementary Fig. 4**). The error of measurement in our approach due to natural refractive index variations in cells was theoretically predicted to be ~3.8 nm for structures positioned 0–350 nm above the substrate (**Supplementary Fig. 5**). These predictions were experimentally validated (**Supplementary Fig. 6**). Lateral resolution in cells was near the limit imposed by diffraction (full width at half maximum, ~300 nm; **Supplementary Fig. 7**).

We used scanning angle interference microscopy to image the vertical positions of cellular structures. Visual reconstructions of dye-labeled, fixed ventral cell membranes revealed fine axial detail, showing distinct topographical features corresponding to the sites of focal adhesion complexes, the cortical actin network proximal to the plasma membrane and the variations in glycocalyx thicknesses of 40–85 nm (**Fig. 1e** and **Supplementary Fig. 8**). In fixed epithelial cells with fluorescently labeled microtubules, the scanning angle interference images showed a downward bending of the microtubule network in the lamella (**Fig. 2a**). Notably, the measured microtubule heights ranged from approximately 70–350 nm, which is beyond the working range of other techniques that offer high axial precision using TIRF.

We next applied scanning angle interference microscopy as a molecular ruler in live cells. We expressed talin, a focal adhesion molecule with a rod-like structure 60 nm in length, as a fusion with mCherry at its N terminus and mEmerald at its

C terminus. We found that the C terminus was situated, on average, 37 nm higher than the N terminus, corresponding to a molecular orientation of 51° relative to the vertical axis. The precision of measurement with our approach was comparable to that achieved with advanced single-molecule localization microscopy methods implemented on two-objective and interference-based microscopes (**Fig. 2b**); however, in contrast to these approaches, our method permits relatively fast acquisition rates of 1–10 s in living cells[8,9]. Scanning angle interference microscopy does not currently incorporate vertical sectioning and is therefore ideally suited for the measurement of discrete structures with nanoscale thickness (<150 nm) (**Supplementary Fig. 9**). For fluorophores distributed vertically in a diffraction-limited spot, it provides an average height of the molecules (**Supplementary Fig. 9**).

Next, we simultaneously measured the heights of paxillin-mEmerald and vinculin-mCherry conjugates, two structural molecules localized to focal adhesions. We observed qualitatively that paxillin increased in height relative to vinculin in the adhesions that formed adjacent to sites of cell-cell contact following the collision of two motile cells (**Fig. 3a** and **Supplementary**

Figure 2 | Scanning angle interference imaging of microtubules and adhesion complexes. (**a**) Epifluorescence image (left) of microtubules in a fixed epithelial cell. The red box marks the region of interest (ROI) shown in the right panels; epifluorescence (top) and the corresponding scanning angle interference image, showing height reconstruction (bottom), are shown. (**b**) The schematic shows dual-labeled talin, which binds integrin and actin through its FERM and THATCH domains, respectively. Bottom left, epifluorescence image of talin. Top and bottom right images show the height of the N terminus and C terminus. Scale bars, 5 µm. Height is reported as the absolute distance of the fluorescent structure above the silicon oxide surface.
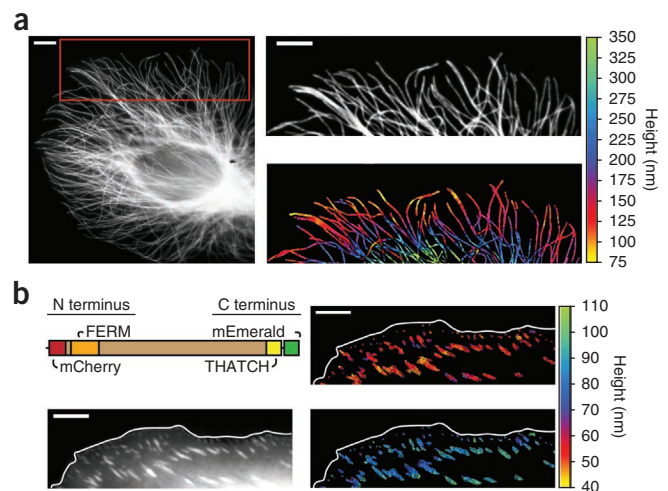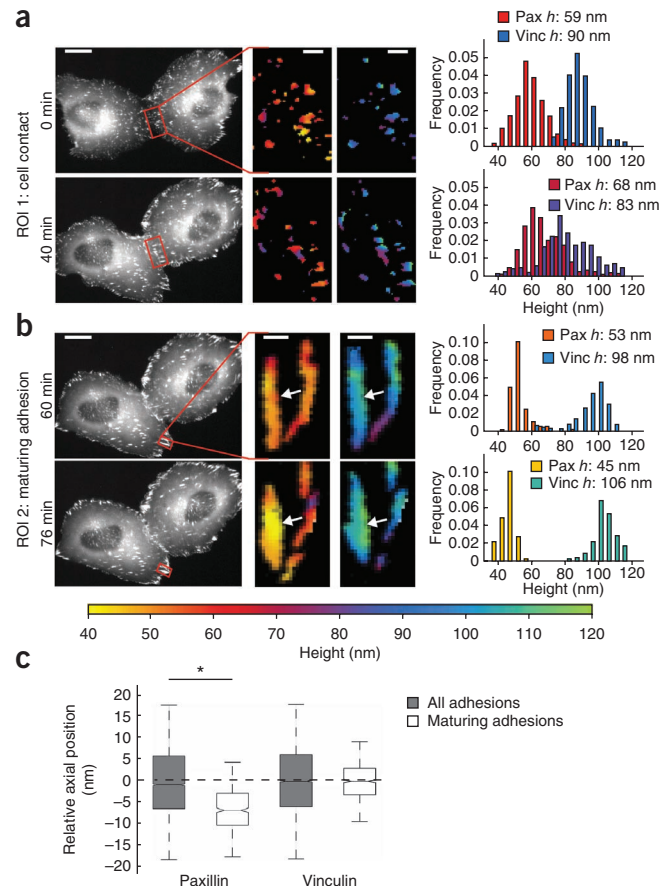
Figure 3 | Nanoscale dynamics of adhesion proteins in migrating cells. (**a**,**b**) Live-cell time-lapse multicolor scanning angle interference imaging of epithelial cells expressing paxillin-mEmerald and mCherry-vinculin (vinc) following cell-cell contact (**a**) or in an assembling adhesion during cell retraction (**b**). The left panels show paxillin epifluorescence images at the indicated time point, and the region of interest (ROI) is boxed in red. Middle and right panels show heights of paxillin and vinculin in the ROI. The plots show distributions of paxillin and vinculin heights in the ROI; mean height (*h*) above the oxide surface is calculated over a range of 35–120 nm. In **a**, the histogram shows the measured heights of paxillin and vinculin at each pixel corresponding to site of adhesion. In **b**, the histogram shows the heights of the molecules at the subset of ROI pixels within the boundary of the left adhesion (indicated by white arrow). Scale bars in **a** and **b**: left, 20 μm; middle and right, 4 μm. (**c**) Relative heights of paxillin and vinculin in randomly selected adhesions that were actively maturing during cell retraction. Axial position is reported relative to the average height of molecules in all adhesions in the cell (*$P < 0.001$; $n = 3$ cells, ≥9 adhesions).

Video 1). In more quantitative measurements, we observed that paxillin and vinculin were vertically stratified in motile cells; paxillin was at an average height of 61 ± 6.5 nm, and vinculin was at an average height of 99 ± 7.2 nm ($P < 0.001$; $n > 20$ cells; **Supplementary Fig. 3**). Finally, we imaged paxillin and vinculin during cycles of cell retraction in the maturing adhesions of motile cells (**Fig. 3b** and **Supplementary Video 1**). Imaging randomly selected adhesions in motile cells revealed that the average height of paxillin in maturing adhesions was significantly lower than that in stable adhesions in nonretracting regions of the cells (**Fig. 3c**), and than that in small, newly formed adhesions in protruding regions ($n = 5$ cells; $P < 0.001$; **Supplementary Fig. 10**). We found that paxillin was typically lowered in maturing adhesions within 5–10 min of the start of cell retraction cycles. In contrast, axial movement of vinculin in maturing adhesions was more random (**Fig. 3c** and **Supplementary Fig. 11**).

Although the mechanism of downward paxillin movement during cell migration remains unclear, one possibility is that these vertical shifts correspond to increased mechanical engagement of the cytoskeleton with the adhesion complex, which is known to stimulate adhesion maturation. Consistent with this notion, we did not observe any downward displacement of paxillin in cells treated with the Rho kinase inhibitor Y-27632 (data not shown).

In summary, we have demonstrated that scanning angle interference microscopy is capable of localizing biological structures with nanoscale precision along the optical axis in living cells on time scales suitable for observing dynamic processes. It will enable the investigation of the many dynamic processes that occur proximal to the cell membrane and should thus be broadly applicable to emerging issues in membrane transport, signal transduction and mechanobiology.

METHODS

Methods and any associated references are available in the online version of the paper.

Note: Supplementary information is available in the online version of the paper.

AUTHOR CONTRIBUTIONS

M.J.P. and V.M.W. conceived and initiated the project. M.J.P. and K.S.T. designed the instrumentation. M.J.P., C.C.D. and M.G.R. designed and performed experiments. M.W.D. designed fluorescent protein constructs. M.J.P. and M.G.R. wrote the analysis software. V.M.W. and J.T.L. supervised the project. All authors wrote the paper.

COMPETING FINANCIAL INTERESTS

The authors declare no competing financial interests.

1. Huang, B., Babcock, H. & Zhuang, X.W. *Cell* **143**, 1047–1058 (2010).
2. Shtengel, G. *et al. Proc. Natl. Acad. Sci. USA* **106**, 3125–3130 (2009).
3. DuFort, C.C., Paszek, M.J. & Weaver, V.M. *Nat. Rev. Mol. Cell Biol.* **12**, 308–319 (2011).
4. Moore, S.W., Roca-Cusachs, P. & Sheetz, M.P. *Dev. Cell* **19**, 194–206 (2010).
5. Parsons, J.T., Horwitz, A.R. & Schwartz, M.A. *Nat. Rev. Mol. Cell Biol.* **11**, 633–643 (2010).
6. Lambacher, A. & Fromherz, P. *J. Opt. Soc. Am. B* **19**, 1435–1453 (2002).
7. Ajo-Franklin, C.M., Ganesan, P.V. & Boxer, S.G. *Biophys. J.* **89**, 2759–2769 (2005).
8. Kanchanawong, P. *et al. Nature* **468**, 580–584 (2010).
9. Xu, K., Babcock, H.P. & Zhuang, X. *Nat. Methods* **9**, 185–188 (2012).

ONLINE METHODS

Preparation of reflective substrates for cell culture. *N*-type (100)-orientation silicon wafers with 500 nm or 1.9 µm of silicon oxide were purchased from Addison Engineering. Wafers with 500 nm or greater silicon oxide were selected to maximize interference contrast (**Supplementary Fig. 12**). Wafers were cut into approximately 1 cm × 1 cm chips by scoring with a diamond-tip pen. They were cleaned by sonicating in acetone for 20 min, rinsing with water, sonicating for 20 min in 1 M potassium hydroxide and rinsing with water. The wafers were then chemically activated to enable conjugation of extracellular matrix proteins for cell adhesion. The wafers were incubated for 1 h in 0.5% (3-aminopropyl) trimethoxysilane (APS) in water, sonicated five times in water for 5 min to remove excess APS, incubated for 1 h in 0.5% glutaraldehyde in phosphate-buffered saline (PBS; pH = 7.4), sonicated five times in water for 5 min and dried under nitrogen gas. The wafers were sterilized under a UV lamp and incubated overnight at 4 °C in 10 µg ml^{-1} human plasma fibronectin (Millipore).

Preparation of reflective substrates with adsorbed nanobeads. To validate the setup, silicon wafers were prepared with defined layers of silicon oxide that functioned as spacers between the silicon surface and adsorbed fluorescent nanobeads on the oxide surface. The SiO$_2$ layers were grown on bare P-type (100)-orientation silicon wafers (Addison Engineering) using silane chemistry (5% SiH$_4$/95% N$_2$) of plasma-enhanced chemical vapor deposition (PECVD process). The plasma was generated by mixing 170 standard cm^3 min^{-1} (sccm) silane (first precursor) and 710 sccm NO$_2$ (second precursor) in an Oxford PlasmaLab 100 system. The NO$_2$ was used as the process oxidant, and its flow rate was enough to obtain high-quality SiO$_2$ films with no excess Si and no Si-H bonding. The chamber pressure was maintained at 1,000 mT. The radio frequency power to generate the plasma of ionized gasses was 20 W. The wafer stage temperature was set at 300 °C, and the chiller control was also set at 70 °C to promote the development of nonporous films. Under these conditions, the silicon oxide deposition rate was 78.6 nm min^{-1}. The thickness of each oxide layer was checked using an n & k 1500 system (n & k Technology). Twenty-nanometer carboxylate-modified yellow-green fluorescent spheres (Invitrogen) were diluted to a final concentration of 5 × 10^8 beads ml^{-1} in PBS plus 100 mM NaCl and sonicated for 5 min to disperse aggregates. Silicon wafers were cut and cleaned as above and incubated in the bead solution for 5 min at room temperature to allow beads to adsorb through hydrophobic interaction. The wafers were then washed once with PBS plus 100 mM NaCl, dried in air at 37 °C and stored at room temperature.

Preparation of fluorescent reference slides. Laser illumination in wide-field epifluorescence is subject to variations in intensity owing to interference fringing. To quantify the variation in intensity, reference slides with a monolayer of fluorescent dye were prepared using silane conjugates of fluorescein and rhodamine B. The conjugates were synthesized by reacting 1 mg of fluorescein isocyanate or 1.37 mg of rhodamine B isocyanate with 9.25 mg of APS in 1.25 ml anhydrous ethanol. Reactions were conducted under nitrogen gas at ~21 °C for 2 h with constant stirring. Immediately following the reaction, the conjugates were centrifuged at 20,000g for 10 min to pellet unwanted aggregates and then diluted ten-fold in absolute ethanol. Clean glass-bottom

dishes (#1.5 glass) were incubated with the diluted silane conjugates for 30 min at ~21 °C, rinsed three times with water and stored in water until imaging.

Lentiviral and expression constructs. To obtain transcriptionally inducible paxillin-mCherry and paxillin-mEmerald, the fusions were cloned into the second-generation lentiviral vector pLV Hygro Tet. pLV Hygro Tet was prepared from pLV tTRKRAB (Addgene #12249) by inserting in place of the EEF1α promoter and tTRKRAB transgene, a hygromycin resistance gene expression cassette consisting of an SV40 promoter and bovine growth hormone polyadenylation sequence in reverse orientation for selection in transduced cells back to back with the regulatable hybrid hepatamerized Tet operator minimal cytomegalovirus (CMV) promoter[10] followed by a central polypurine tract and the multiple cloning site (MCS) from pcDNA3.1+ (Invitrogen). The paxillin-mCherry gene was excised from a N1 Clontech-style vector with the restriction enzymes Nhe-I (made blunt) and Not-I and inserted into the PME-I and Not-I sites of the pLV Hygro Tet MCS to make pLV paxillin–mCherry Hygro Tet. Similarly, paxillin-mEmerald was cloned to make pLV paxillin–mEmerald Hygro Tet. A second lentiviral construct, pLV rtTA^s-M2 IRES Neo, was also prepared from pLV tTRKRAB to provide EEF1α promoter–mediated constitutive expression of the synthetic tetracycline inducible reverse transcriptional transactivator rtTA^s-M2) from a bicistronic mRNA coexpressing neomycin phosphotransferase downstream of an internal ribosome entry site for selection of transduced cells with G418. The structure and sequence of pLV Hygro Tet, pLV paxillin–mCherry Hygro Tet, pLV paxillin–mEmerald Hygro Tet and pLV rtTA^s-M2 IRES Neo are available for download at https://www.lablife.org/ll (Weaver lab).

A validated short hairpin RNA interference oligonucleotide (TRCN0000299022) in the lentivector pLKO.1 Puro targeting the human Talin1 3′ UTR was obtained from Sigma. Mouse Talin1 tagged with mCherry at the N terminus and mEmerald at the C terminus was prepared from previously described mouse Talin1 constructs tagged with mCherry at the N terminus and mEmerald at the C terminus[8]. A SalI-NotI fragment from the mEmerald construct containing the C-terminal end of Talin1 fused to mEmerald was ligated to a AgeI-SalI fragment from the mCherry construct containing mCherry fused to the N-terminal end of Talin1 and a NotI-AgeI vector fragment from pmCherry-N1 (Clontech). Mouse Talin1 tagged at its N and C termini with mCherry was prepared from this latter construct by substituting an AgeI-NotI mCherry fragment from pmCherry-N1 for mEmerald. The construct for expression of mCherry-vinculin (C-terminal fusion) was described previously[11].

Cell culture and imaging sample preparation. MCF10A human mammary epithelial cells were grown at 37 °C and 5% CO$_2$ in DMEM F12 (Invitrogen) supplemented with 5% donor horse serum (Invitrogen), 20 ng ml^{-1} epidermal growth factor (Peprotech), 10 µg ml^{-1} insulin (Sigma), 0.5 µg ml^{-1} hydrocortisone (Sigma), 0.1 µg ml^{-1} cholera toxin (Sigma) and 100 U ml^{-1} penicillin-streptomycin. For stable expression of paxillin-mEmerald or paxillin-mCherry, recombinant lentivirus was prepared by transient transfection into HEK-293T cells and used to transduce MCF10A cells as previously described[12]. Stable cell lines were selected in 200 ng ml^{-1} G418 and 380 ng ml^{-1} hygromycin and

sorted on a FACSAria II cell sorter (BD Biosciences) for paxillin-mEmerald or paxillin-mCherry expression. Expression of paxillin-mEmerald or paxillin-mCherry was induced with 200 ng ml^{-1} doxycycline in growth medium for 1 d before experimentation. Transient transfection was with Lonza Nucleofector Kit V (program T024). Talin fluorescent protein conjugates were cotransfected with shRNA targeting endogenous MCF10A talin1.

For all experiments, cells were replated on fibronectin-conjugated silicon wafers and cultured overnight before live-cell imaging, fixation or cell roofing. Except for those used in microtubule imaging, cells were plated on wafers with 500 nm silicon oxide, and fixation was performed in 2% paraformaldehyde for 20 min. For cell membrane imaging, the dorsal cell membrane was removed through cell roofing according to previously described protocols[13]. Briefly, cells were swelled in ice-cold hypotonic buffer (15 mM KCl, 15 mM HEPES, 1 mM CaCl$_2$, 1 mM MgCl$_2$, pH 7.4) for 4 min. Swollen cells were then sonicated with a probe-type sonicator (Microson XL2000; Misonix) using a short pulse (<1 s, power setting 8) with the sonicator probe (1/8 inch diameter) approximately 3 mm above the cells. Following sonication, the remaining ventral plasma membranes were rinsed once in PBS and fixed. Membranes were labeled with fluorescent dye after fixation by incubating in 1 µM Vybrant DiO (Invitrogen) in PBS for 1 h at room temperature. Rho kinase inhibition was with 10 µM of the inhibitor Y-27632 (Cayman Chemical) in growth medium. For the microtubule imaging, cells were plated on wafers with 1.9 µm silicon oxide overnight and fixed by incubating in 0.25% glutaraldehyde for 30 s and then transferring them to a solution of 0.25% glutaraldehyde with 0.1% Triton X-100 in PBS. Cells were then rinsed with PBS and covered with a freshly prepared drop of 0.2% sodium borohydride in PBS, which was exchanged three times over 30 min. This was followed by two rinses with PBS and a 10-min incubation with a solution of PBS, 2% BSA and 0.1% Triton X-100. Microtubules were labeled with rat monoclonal tubulin-specific antibody (AbD Serotec; Clone YL1/2; 2 µg ml^{-1} final concentration) and Alexa488-conjugated rat-specific secondary antibody (Invitrogen; 5 µg ml^{-1} final concentration).

Image acquisition. Imaging was performed on a motorized objective-type TIRF inverted microscope system (Ti-E Perfect Focus System; Nikon) equipped with 488-nm and 561-nm lasers, electronic shutters and an electron-multiplying charged-coupled device camera (QuantEM 512; Photometrics) and controlled by NIS-Elements software (Nikon). A linear glass polarizing filter (Edmunds Optics) was placed in the excitation laser path to polarize the light perpendicular to the plane of incidence, along which the excitation laser light emanates from the objective. On the Nikon microscope, the polarizer was placed in the filter cube housing the dichroic mirror, where the excitation filter would normally sit. The relationship between the motor position of the TIRF illuminator and the actual angle of laser light out of the objective was calibrated by varying motor position and measuring the position of the focused laser spot along the ceiling of the room housing the microscope or with a protractor. The corresponding angles in aqueous samples were determined from Snell's Law. Motor units corresponding to desired laser incidence angles for image acquisition were programmed into NIS-Elements to facilitate automated data acquisition. Samples were imaged with a 60×/NA 1.2 water-immersion objective (CFI Plan Apo VC;

Nikon) or a 100×/NA 1.45 oil-immersion objective (CFI Plan Apo Lambda; Nikon) with additional magnification using a 1.5× optovar (0.18 µm per pixel for 60×, 0.11 µm per pixel for 100×). Silicon substrates were placed sample side down in 35-mm #1.5 glass-bottom dishes in PBS or phenol red-free growth medium with 10 mM HEPES (pH 7.4) to maintain pH for live-cell imaging. A buoyancy-adjusted weight of approximately 1.75 g was placed on the wafer to keep the wafer sample surface flat against the glass bottom. Live cells were maintained at 37 °C using a blower-style heater (ASI 400; Nevtek). For imaging microtubules on silicon substrates with 1.9 µm of silicon oxide, a sequence of 35 epifluorescence images of each sample was obtained by scanning through laser incidence angles below the critical angle from −34° to +34° in 2° increments along the plane of incidence (**Supplementary Fig. 12**). For all other samples, a sequence of 27 epifluorescence images was obtained from −52° to +52° in 4° increments. Typical camera exposure times were on the order of 10–100 ms (with an electron multiplying gain of 200), resulting in acquisition rates on the order of 3–60 s per image sequence. A sequence of images of the reference slides was obtained similarly for each color channel.

Optical theory. The electromagnetic theory describing silicon surface-generated standing waves of excitation radiation has previously been reported[14]. The layered silicon oxide–silicon structure is treated as a single virtual layer using transfer matrix methods that account for internal reflections and refractions. Reflection and refraction at known sample interfaces, including the cell membrane and sample buffer or the cell membrane and cell cytoplasm, were determined to have a negligible effect on the structure of the electric field and were therefore excluded from the optical theory (**Supplementary Fig. 13**). For incident light polarized perpendicular to the plane of incidence, the relative local electric field at a position H in the sample above the silicon oxide is given by

$$F \sim 1 + r^{TE}e^{i\phi(H)} \tag{1}$$

where r^{TE} is the transverse electric (TE) component, perpendicular to the plane of incidence, of the Fresnel coefficient of reflection between the sample interface and the virtual silicon oxide–silicon layer, and ϕ is the phase difference of the direct and reflected light at axial position H given by

$$\phi(H) = \frac{4\pi}{\lambda}\left(n_b H \cos\theta_b\right) \tag{2}$$

The effective Fresnel coefficient is obtained from the characteristic transfer matrix m^{TE} according to

$$r^{TE} = \frac{\left(m_{11}^{TE} + m_{12}^{TE}p_o\right)p_2 + \left(m_{21}^{TE} - m_{22}^{TE}p_o\right)}{\left(m_{11}^{TE} + m_{12}^{TE}p_o\right)p_2 + \left(m_{21}^{TE} + m_{22}^{TE}p_o\right)} \tag{3}$$

$$
\begin{aligned}
M_{TE} &= \begin{pmatrix} m_{11}^{TE} & m_{12}^{TE} \\ m_{21}^{TE} & m_{22}^{TE} \end{pmatrix} \\
&= \begin{pmatrix} \cos(k_{ox}d_{ox}\cos\theta_{ox}) & -\dfrac{i}{p_1}\sin(k_{ox}d_{ox}\cos\theta_{ox}) \\ -ip_1\sin(k_{ox}d_{ox}\cos\theta_{ox}) & \cos(k_{ox}d_{ox}\cos\theta_{ox}) \end{pmatrix}
\end{aligned} \tag{4}
$$

$$p_o = n_{Si} \cos\theta_{Si}, \; p_1 = n_{ox} \cos\theta_{ox}, \; p_2 = n_b \cos\theta_b \qquad (5)$$

$$k_i = \frac{2\pi n_i}{\lambda} \qquad (6)$$

where k_i is the wavenumber in material i; n_{Si}, n_{ox} and n_b are the refractive index of the silicon, silicon oxide and sample, respectively; θ_{Si}, θ_{ox} and θ_b are the angles of incidence in the silicon, silicon oxide and sample, respectively; and d_{ox} is the thickness of the silicon oxide layer. The angles of incidence in silicon oxide and silicon were calculated according to Snell's Law.

Image analysis. For height reconstructions, intensity profiles from acquired image sequences were fit to the optical theory on a pixel-by-pixel basis. To correct for uneven laser illumination across the image, the intensity of each pixel (and for live-cell imaging, an all-pixel average) in each sample image was adjusted according to the corresponding intensity in the reference slide image sequence

$$I_{i,n} = \frac{S_{i,n} - C}{R_{i,n} - C} \qquad (7)$$

where $S_{i,n}$ is the intensity of pixel i in sample image n, $R_{i,n}$ is the intensity of pixel i in reference image n and C is the average background intensity of the camera device obtained by snapping an image on the microscope with the shutters closed and averaging the intensity over all image pixels. Emission by fluorophores on the microscope is proportional to the excitation radiation intensity, which is proportional to the square of equation (1). The detected pattern of intensity variation at a given pixel in the sample image sequence was thus fit according to

$$I = A\left|1 + r^{TE} e^{i\phi(H)}\right|^2 + B \qquad (8)$$

Here the scaling parameter A accounts for variation in detected intensity due to factors including mean excitation laser intensity, fluorophore density, fluorophore photophysics, self-interference of emitted photons and efficiency of emitted photon detection. The offset parameter B accounts for background fluorescence in the sample images. Parameters A, B and H were fit through constrained nonlinear least-squares optimization using Trust Region algorithms (Math Kernel Library; Intel). Fitted data whose scaling parameter was below a defined minimum (for example, dim structures) were excluded from further analysis.

Software. A custom software package for image analysis and height reconstruction of scanning angle interference image sequences was written in C++ and compiled for the Linux operating system. Additional programs for data analysis and three-dimensional visualization were written in Matlab and Python using libraries distributed by Enthought, Inc.

10. Gossen, M. & Bujard, H. *Proc. Natl. Acad. Sci. USA* **89**, 5547–5551 (1992).
11. Burnette, D.T. *et al. Nat. Cell Biol.* **13**, 371–381 (2011).
12. Barde, I., Salmon, P. & Trono, D. *Curr. Prot. Neurosci.* **53**, 4.21.1–4.21.23 (2010).
13. Drees, F., Reilein, A. & Nelson, W.J. *Methods Mol. Biol.* **294**, 303–320 (2005).
14. Lambacher, A. & Fromherz, P. *Appl. Phys. A* **63**, 207–216 (1996).